

Comparative Analysis of the Near- and Far-Field Optical Response of Thin Plasmonic Nanostructures

Lauren Zundel, Paul Gieri, Stephen Sanders, and Alejandro Manjavacas*

Nanostructures made of metallic materials support collective oscillations of their conduction electrons, commonly known as surface plasmons. These modes, whose characteristics are determined by the material and morphology of the nanostructure, couple strongly to light and confine it into subwavelength volumes. Of particular interest are metallic nanostructures for which the size along one dimension approaches the nanometer or even the subnanometer scale, since such morphologies can lead to stronger light–matter interactions and higher degrees of confinement than regular three-dimensional nanostructures. Here, the plasmonic response of metallic nanodisks of varying thicknesses and aspect ratios is investigated under far- and near-field excitation conditions. It is found that, for far-field excitation, the strength of the plasmonic response of the nanodisk increases with its thickness, as expected from the increase in the number of conduction electrons in the system. However, for near-field excitation, the plasmonic response becomes stronger as the thickness of the nanodisk is reduced. This behavior is attributed to the higher efficiency with which a near-field source couples to the plasmons supported by thinner nanodisks. The results of this work advance the understanding of the plasmonic response of thin metallic nanostructures, thus increasing their potential for the development of novel applications.

plasmons are being exploited to develop applications as diverse as ultrasensitive optical sensing,^[4–6] efficient solar energy harvesting,^[7,8] photocatalysis,^[9,10] and nanoscale light emission,^[11,12] to cite a few.

In recent years, the isolation of graphene^[13] and the discovery of the extraordinary plasmonic properties this material has when doped with carriers^[14–19] has inspired significant interest in studying the plasmons supported by metallic nanostructures with thicknesses ranging from several nanometers down to monolayers.^[20–34] These nanostructures support very strong fields that lead to increased light–matter interaction^[14,24,35–39] and produce a higher degree of confinement than regular 3D structures, enabling, for instance, the enhancement of higher-order multipolar transitions.^[40–42] Furthermore, the reduced dimensionality of these nanostructures makes it easier to modify their optical response by altering their distribution of free carriers, as has been both theoretically proposed^[21,43] and experimentally demonstrated.^[44]


1. Introduction

Metallic nanostructures are known to support surface plasmons, collective oscillations of their conduction electrons,^[1] which couple strongly to electromagnetic radiation, confine it into subwavelength volumes, and produce large field enhancements around the nanostructure.^[2,3] Thanks to these abilities, surface

When analyzing the optical response of a metallic nanostructure, we can distinguish two different regimes depending on the position of the source with respect to the nanostructure. Specifically, far-field excitation corresponds to the situation in which the distance d between them is much larger than the wavelength λ , while the opposite limit (i.e., $d \ll \lambda$) is known as near-field excitation. The former scenario applies when the nanostructure is excited by a propagating electromagnetic field and, therefore, is relevant for applications centered on controlling the propagation of electromagnetic radiation, as is the case for metasurfaces,^[45] improved solar energy harvesting devices,^[46] and photocatalysis,^[10] to cite a few. On the other hand, near-field excitation occurs when the nanostructure is excited by a localized source, such as an atom, molecule, or quantum dot, placed in its vicinity. Therefore, characterizing this regime is important for applications in which the nanostructure is used to enhance and control the interaction between localized emitters and light.^[47–50] Importantly, far- and near-field sources are, in general, not able to excite every single mode of the nanostructure. A paradigmatic example is the so-called dark modes, whose name originates from the fact that, due to their symmetry, they are not efficiently excited by propagating electromagnetic fields.^[51,52] Because of this, and since many applications, such as ultrasensitive optical sensing, involve both far- and near-field excitation, a complete

L. Zundel, P. Gieri, S. Sanders, A. Manjavacas
Department of Physics and Astronomy
University of New Mexico
Albuquerque, NM 87106, USA
E-mail: a.manjavacas@csic.es

A. Manjavacas
Instituto de Óptica (IO-CSIC)
Consejo Superior de Investigaciones Científicas
Madrid 28006, Spain

 The ORCID identification number(s) for the author(s) of this article can be found under <https://doi.org/10.1002/adom.202102550>.

© 2022 The Authors. Advanced Optical Materials published by Wiley-VCH GmbH. This is an open access article under the terms of the Creative Commons Attribution-NonCommercial License, which permits use, distribution and reproduction in any medium, provided the original work is properly cited and is not used for commercial purposes.

DOI: 10.1002/adom.202102550

understanding of both the near- and far-field optical response of metallic nanostructures is essential to leverage their full potential.

Here, we investigate how the thickness of a metallic nanostructure affects its near- and far-field optical response. To that end, we present rigorous solutions of Maxwell's equations for metallic nanodisks under near- and far-field excitation as a function of the thickness of the nanodisk when either its aspect ratio or cross-sectional area is kept fixed. In both cases, we find that the strength of the far-field response of the nanodisks increases with their thickness, a result that is anticipated due to the increased volume and therefore larger number of carriers present in the nanostructure. In sharp contrast, the near-field response of the nanodisks decreases with thickness, a behavior that we attribute to the larger coupling to near-field sources displayed by thinner nanodisks. Our results shed light into the plasmonic response of thin metallic nanostructures and thus pave the way toward applications such as highly-integrated electro-optical modulators, for which low-dimensional systems are ideal due to their increased susceptibility to the modulation of their optical response.^[21,44]

2. Results and Discussion

The system under consideration is a metallic nanodisk of thickness t and diameter D , lying in the xy -plane and surrounded by vacuum, as depicted in the insets of Figure 1a,b. Since we are interested in analyzing the optical response

arising from the plasmon resonances supported by the nanodisk, we describe its dielectric function using a Drude model $\epsilon(\omega) = 1 - \omega_p^2 / (\omega^2 + i\omega\gamma)$, with $\hbar\omega_p = 6\text{ eV}$ and $\hbar\gamma = 0.06\text{ eV}$. However, we later extend our calculations to analyze the role played by interband transitions by using a tabulated dielectric function. All of the results shown in this work are obtained by rigorously solving Maxwell's equations using the finite element method (FEM) (see Supporting Information for details about the FEM calculations). Moreover, all of the nanodisks that we consider in this work have sufficiently large dimensions that nonlocal and quantum effects play a minor role.^[21,32]

We first consider the response of the nanodisks to far-field excitation by a plane wave that is linearly polarized along the x -axis and propagates in the z -direction. Specifically, we calculate the extinction cross-section $\sigma_{\text{ext}}(\omega)$, which quantifies the fraction of light that is either scattered or absorbed by the nanodisk. The results of this calculation, normalized to the area of the nanodisks $A = \pi D^2/4$, are plotted in Figure 1a. The gray curve shows $\sigma_{\text{ext}}(\omega)/A$ for a nanodisk with $t = 2\text{ nm}$ and $D = 50\text{ nm}$, which supports a strong dipolar resonance, with a peak value of ≈ 5.59 located at an energy of $\hbar\omega \approx 1.17\text{ eV}$. To analyze how $\sigma_{\text{ext}}(\omega)/A$ changes with the thickness of the nanodisk, we first vary t while holding $D = 50\text{ nm}$ constant. Doing so results in an increase of the extinction cross-section, as shown with blue, cyan, and green curves for $t = 5, 10,$ and 20 nm , respectively. At the same time, the energy of the resonance blueshifts significantly, with the $t = 20\text{ nm}$ nanodisk having its first mode at $\hbar\omega \approx 2.54\text{ eV}$. We can avoid the blueshift in the

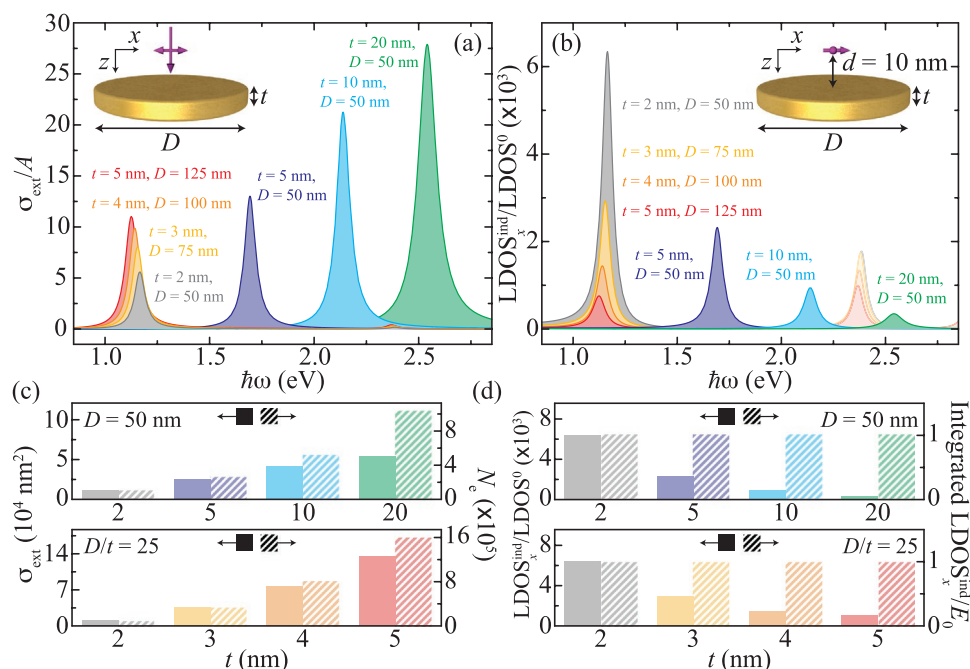


Figure 1. Far- and near-field optical response of metallic nanodisks as a function of their thickness. a) Extinction cross-section $\sigma_{\text{ext}}(\omega)$, normalized to the cross-sectional area $A = \pi D^2/4$, for nanodisks of diameter D and thickness t , under illumination by a plane wave, as depicted in the inset schematics. b) Induced LDOS calculated at a distance $d = 10\text{ nm}$ above the center of the surface of the nanodisk, as shown in the schematics, normalized to the LDOS of vacuum, $\text{LDOS}_x^0(\omega) = \omega^2 / (3\pi^2 c^3)$, for the same nanodisks as in (a). c) Peak value of $\sigma_{\text{ext}}(\omega)/A$ (solid bars, left axis) and number of conduction electrons in the nanodisk N_e (striped bars, right axis) as a function of t . d) Peak value of the normalized LDOS $\text{LDOS}_x^{\text{ind}}(\mathbf{r}, \omega)$ (solid bars, left axis) and value of the integrated LDOS $\text{integrated LDOS}_x^{\text{ind}}(\mathbf{r}, \omega)$ divided by E_0 (striped bars, right axis) as a function of t . In both (c) and (d), the upper plot corresponds to the nanodisks with constant diameter, while the lower one shows the results for the nanodisks with fixed aspect ratio.

resonance energy by, instead, increasing t and D simultaneously, keeping a fixed aspect ratio. This case is shown by the yellow, orange, and red curves, which display, respectively, the normalized extinction cross-section for nanodisks with $t = 3, 4,$ and 5 nm and an aspect ratio of $D/t = 25$. In the electrostatic limit, the resonance energy of a nanodisk depends only on its aspect ratio and not on its overall size.^[53] However, for the nanodisks under consideration here, there is a slight redshift of the resonance energy that grows with their size and, therefore, we attribute it to the effect of retardation.

When the nanodisks of Figure 1a are instead subject to near-field excitation, their response is drastically different. In order to characterize it, we use the local density of photonic states (LDOS), which, as expected from its name, quantifies the number of photonic states per unit of frequency and volume for a given system.^[54–59] This quantity also describes the modification of the decay rate of an emitter due to the presence of the nanodisk and thus adequately measures the response of the system to near-field excitation.^[54,60,61] Using Gaussian units, the LDOS projected along the direction \hat{n} at a point \mathbf{r} is given by^[54,59]

$$\text{LDOS}_{\hat{n}}(\mathbf{r}, \omega) = \frac{1}{2\omega\pi^2} \text{Im}\{\hat{n} \cdot \mathbf{G}(\mathbf{r}, \mathbf{r}, \omega) \cdot \hat{n}\} \quad (1)$$

where $\mathbf{G}(\mathbf{r}, \mathbf{r}', \omega)$ is the Green tensor of Maxwell's equations, defined as the solution of

$$\nabla \times \nabla \times \mathbf{G}(\mathbf{r}, \mathbf{r}', \omega) - k^2 \varepsilon(\mathbf{r}, \omega) \mathbf{G}(\mathbf{r}, \mathbf{r}', \omega) = 4\pi k^2 \delta(\mathbf{r} - \mathbf{r}') \mathbf{I} \quad (2)$$

with $\varepsilon(\mathbf{r}, \omega)$ being the dielectric function of the system and $k = \omega/c$ the wave number. In our particular case, we are interested in the response of the nanodisk when excited by an x -polarized dipole placed a distance d above the center of its surface, as depicted in the schematics of Figure 1b. Therefore, we focus on the induced part of the LDOS projected along the x -axis, which, normalized to the LDOS of vacuum, $\text{LDOS}^0(\omega) = \omega^2/(3\pi^2 c^3)$, can be calculated as

$$\frac{\text{LDOS}_x^{\text{ind}}(\mathbf{r}, \omega)}{\text{LDOS}^0(\omega)} = \frac{3}{2k^3} \text{Im}\{G_{xx}^{\text{ind}}(\mathbf{r}, \mathbf{r}, \omega)\} \quad (3)$$

Here, $G_{xx}^{\text{ind}}(\mathbf{r}, \mathbf{r}, \omega)$ represents the xx -component of the induced part of the Green tensor, that is, the contribution to the Green tensor solely due to the nanodisk without that of vacuum. Importantly, with the definition of $\mathbf{G}(\mathbf{r}, \mathbf{r}', \omega)$ that we use here (which differs by a factor of $-4\pi\omega^2$ from our previous work^[59]), $G_{xx}^{\text{ind}}(\mathbf{r}, \mathbf{r}, \omega)$ is exactly the x -component of the field produced by the nanodisk at a position \mathbf{r} in response to an x -polarized unit dipole located at that position.

The spectrum of the induced LDOS for $d = 10$ nm is shown in Figure 1b for the same nanodisks analyzed in Figure 1a. Clearly, all of them display a strong peak located at approximately the same spectral position as the extinction peak. Interestingly, higher-order dipolar modes that were not efficiently excited by the plane wave are also visible in the spectra of the nanodisks with fixed aspect ratio, although, here, we restrict our analysis only to the first dipolar mode (see Figure S1, Supporting Information for an analysis of the higher-order dipolar modes of the nanodisks). Importantly, in sharp contrast with the behavior of the extinction cross-section, the induced LDOS decreases as the thickness of

the nanodisk grows, both for the nanodisks with fixed diameter $D = 50$ nm and for those with fixed aspect ratio $D/t = 25$.

We analyze these opposing trends in more detail in Figure 1c,d. Specifically, in Figure 1c, we plot, using solid bars and the left scale, the peak value of $\sigma_{\text{ext}}(\omega)$ for all of the nanodisks in Figure 1a. The upper and lower plots show, respectively, the results for the nanodisks with fixed diameter and fixed aspect ratio. As discussed before, in all of the cases, the peak value of $\sigma_{\text{ext}}(\omega)$ grows with t , a behavior that is completely consistent with the Thomas–Reiche–Kuhn sum rule.^[62–64] This sum rule, also known as the f -sum rule, states that the integral over frequencies of the extinction cross-section of a nanostructure made of a material that can be described by a local, causal, and linear dielectric function satisfies^[64]

$$\int_0^\infty d\omega \sigma_{\text{ext}}(\omega) = \frac{2\pi^2 e^2}{m_e c} N_e \approx 1.67 \times 10^{-5} N_e [\text{m}^2 \text{s}^{-1}] \quad (4)$$

with m_e and e being the electron mass and charge, respectively. Applied to our nanodisks, this means that their integrated extinction cross-section is proportional to the number of conduction electrons N_e that they contain and hence to their volume. Since the spectrum of $\sigma_{\text{ext}}(\omega)$ is dominated by the lowest-order dipolar mode, the same behavior can be expected for its peak value.

The striped bars and right scale of Figure 1c show the value of N_e computed from the plasma frequency ω_p that we use for the dielectric function of the nanodisks $N_e = m_e \omega_p^2 A t / (4\pi e^2)$. We have checked these results numerically by directly computing the integral of the extinction cross-section over a sufficient range of frequencies. Interestingly, comparing N_e and the peak value of $\sigma_{\text{ext}}(\omega)$, we observe that the former quantity grows more quickly with t , which indicates that both the contribution of higher-order modes to the extinction spectrum as well as the width of the resonances increase for the thicker nanodisks.

We can apply a similar analysis to the near-field response studied in Figure 1b since, as shown in ref. [59], the LDOS induced by the nanodisks also satisfies a sum rule

$$\int_0^\infty d\omega \text{LDOS}_x^{\text{ind}}(\mathbf{r}, \omega) = \frac{E_x^{\text{ind}}(\mathbf{r})}{4\pi} \quad (5)$$

with $E_x^{\text{ind}}(\mathbf{r})$ being the x -component of the field at position \mathbf{r} produced by an x -polarized, static (i.e., for $\omega = 0$), unit dipole located at that position, due to the presence of the nanodisk. Figure 1d compares the peak value of the normalized $\text{LDOS}_x^{\text{ind}}(\mathbf{r}, \omega)$ (left scale, solid bars) with the integrated $\text{LDOS}_x^{\text{ind}}(\mathbf{r}, \omega)$ (right scale, striped bars) divided by $E_0 = (32\pi(10 \text{ nm})^3)^{-1}$. This quantity is $(4\pi)^{-1}$ times the electric field produced, at its own position, by an x -polarized, static, unit dipole placed a distance $d = 10$ nm from a semi-infinite, perfectly conducting, medium. For the systems under consideration here, which satisfy $D \gg d$, $4\pi E_0$ is an excellent approximation of $E_x^{\text{ind}}(\mathbf{r})$,^[59] as we have confirmed numerically by integrating the induced LDOS. Importantly, this also means that the integrated $\text{LDOS}_x^{\text{ind}}(\mathbf{r}, \omega)$ has a constant value for all of the nanodisks under consideration, in sharp contrast with the peak value of the $\text{LDOS}_x^{\text{ind}}(\mathbf{r}, \omega)$, which clearly decreases as t grows. Therefore, while the sum rule of the extinction cross-section and its peak value have a consistent behavior as the thickness of the nanodisk is varied, that is not

the case for the induced LDOS. This highlights the more complex behavior of the near-field response and motivates the further analysis we present below.

One aspect of the optical response that can give additional insight is the induced charge on the nanodisks, which we analyze in Figure 2. Specifically, in Figure 2a, we show the spatial distribution of the induced charge on the nanodisks with $t = 2$ nm and $D = 50$ nm (gray outlines), $t = 5$ nm and $D = 125$ nm (red outlines), and $t = 20$ nm and $D = 50$ nm (green outlines) under both plane wave illumination (upper plots) and dipole excitation at $d = 10$ nm (lower plots). In all cases, the charge distributions are calculated at the energy of the first peak in the corresponding spectrum and the color scale is saturated to $\pm 80\%$ of its maximum magnitude. Clearly, the charge distributions of all of the nanodisks show a dipolar pattern and are identical for near- and far-field excitation, thus confirming that, in both cases, the first peak in the spectrum corresponds to the lowest-order dipolar plasmon.

In order to gain further insight, we analyze the total induced charge in the nanodisks, which is shown in Figure 2b,c for the

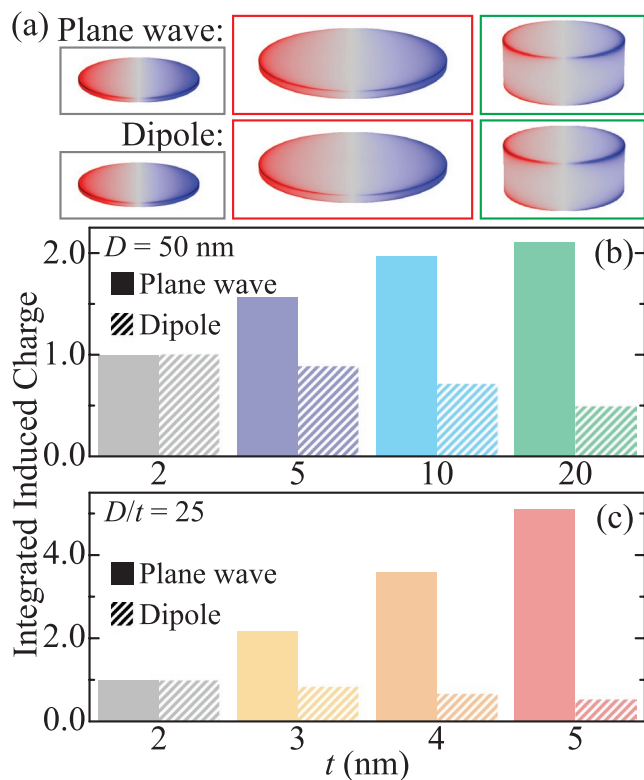


Figure 2. Induced charge in metallic nanodisks as a function of their thickness. a) Spatial profile of the induced charge in nanodisks with $t = 2$ nm, $D = 50$ nm (gray outline), $t = 5$ nm, $D = 125$ nm (red outline), and $t = 20$ nm, $D = 50$ nm (green outline) under excitation by either a plane wave (top row) or a dipole placed $d = 10$ nm from the center of the surface of the nanodisk (bottom row). b,c) Integrated induced charge for metallic nanodisks with varying t and either $D = 50$ nm or $D/t = 25$. Solid and striped bars correspond to excitation by the plane wave and dipole, respectively. In all cases, the induced charge is calculated at the energy of the first peak of the corresponding spectra shown in Figure 1. Furthermore, all of the integrated induced charges are normalized to those of the $t = 2$ nm nanodisk with the same excitation source.

nanodisks with $D = 50$ nm and $D/t = 25$, respectively. In both cases, solid bars represent the results for the plane wave excitation, while striped bars correspond to the dipole excitation. Since the nanodisks are electrically neutral, the induced charge over the entire surface must be zero. Therefore, we integrate the absolute value of the charge over the entire surface. Moreover, since the overall value depends on the strength of the excitation source, we normalize all of the calculations to the value obtained for the $t = 2$ nm nanodisk excited by the same source.

As expected from the growth in the extinction, when the dipolar plasmon of the nanodisks is excited by a plane wave, the total induced charge grows with t . For the nanodisks with $D/t = 25$, this growth is much more rapid, with the $t = 5$ nm, $D = 125$ nm (red) nanodisk having approximately a fivefold enhancement over the $t = 2$ nm nanodisk (gray). This can be attributed to the fact that, for the fixed aspect ratio, all of the dimensions of the nanodisk are simultaneously increased. In contrast, when the nanodisks are excited by a dipole, the charge decreases as the size of the nanodisks grows, with both the $t = 5$ nm, $D = 125$ nm (red) and the $t = 20$ nm, $D = 50$ nm (green) nanodisks having approximately half of the total induced charge as the $t = 2$ nm one. Since the strength of the dipolar plasmon of the nanodisks is expected to increase with their number of free carriers, and therefore their volume, these results suggest that the trend with thickness observed for the near-field excitation scenario has to be connected to the efficiency with which a near-field source excites the dipolar plasmon of the nanodisks. This efficiency is ultimately determined by the spatial distribution of the electromagnetic fields of the source and the plasmon of the nanodisk.

In order to explore this hypothesis, we analyze, in Figure 3a, the near-field response of the nanodisks as we vary the distance separating them from the dipole source. In particular, we focus on nanodisks with $t = 2$ nm, $D = 50$ nm (gray dots), $t = 5$ nm, $D = 125$ nm (red dots), and $t = 20$ nm, $D = 50$ nm (green dots), and calculate the peak value of $\text{LDOS}_x^{\text{ind}}(\mathbf{r}, \omega)$ as a function of d at the energy corresponding to the first dipolar plasmon for $d = 10$ nm (see Figure 1b). As expected, in all cases, the induced LDOS decreases rapidly with d , although this does not happen at the same rate for the different nanodisks. Indeed, although the thinnest nanodisk displays the largest induced LDOS for all the distances under consideration, its value approaches that of the $t = 5$ nm, $D = 125$ nm nanodisk as d grows. It is worth noting that a similar behavior occurs for metallic nanospheres^[65] and ellipsoids.^[58]

Interestingly, it is possible to explain these trends by calculating an approximate value of the induced LDOS within the dipolar and electrostatic limits. Specifically, assuming that the nanodisk can be modeled as a point dipole with polarizability $\alpha(\omega)$ located at \mathbf{r}' , we can approximate $\text{Im}\{G_{xx}^{\text{ind}}(\mathbf{r}, \mathbf{r}, \omega)\} \approx \text{Im}\{G_{xx}^0(\mathbf{r}, \mathbf{r}', \omega)\alpha(\omega)G_{xx}^0(\mathbf{r}', \mathbf{r}, \omega)\}$. Here, $G_{xx}^0(\mathbf{r}, \mathbf{r}', \omega)$ represents the vacuum Green tensor connecting points \mathbf{r} and \mathbf{r}' , which, in the electrostatic limit $k|\mathbf{r} - \mathbf{r}'| \ll 1$, reduces to $G_{xx}^0(\mathbf{r}, \mathbf{r}') \approx 3(x - x')^2 / |\mathbf{r} - \mathbf{r}'|^5 - 1 / |\mathbf{r} - \mathbf{r}'|^3$. Therefore, using these expressions, we can approximate Equation (3) as

$$\frac{\text{LDOS}_x^{\text{ind}}(\mathbf{r}, \omega)}{\text{LDOS}^0(\omega)} \approx \frac{3\text{Im}\{\alpha(\omega)\}}{2k^3} [G_{xx}^0(\mathbf{r}, \mathbf{r}')^2] \quad (6)$$

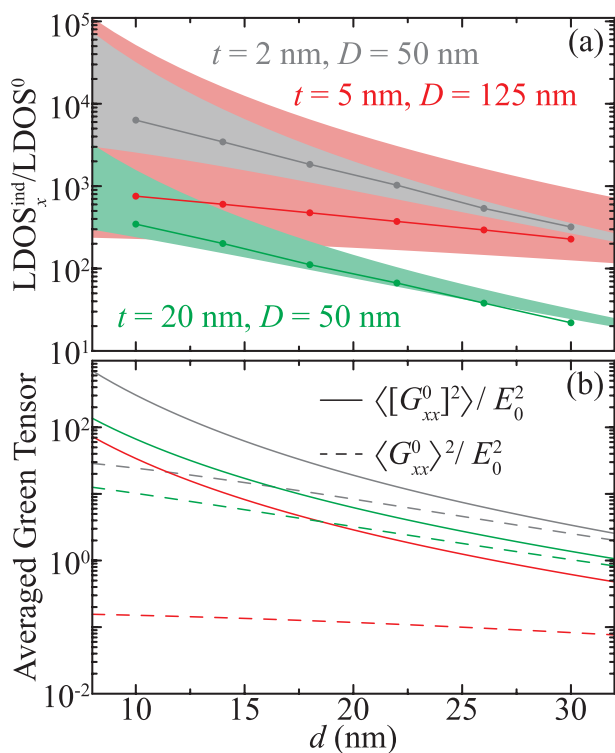


Figure 3. Analysis of the excitation of nanodisks by a dipole source. a) Normalized $\text{LDOS}_x^{\text{ind}}(\mathbf{r}, \omega)$ at resonance for nanodisks with $t = 2$ nm, $D = 50$ nm (gray dots), $t = 5$ nm, $D = 125$ nm (red dots), and $t = 20$ nm, $D = 50$ nm (green dots) calculated at a distance d above the center of the surface of the nanodisk. The shaded areas represent the values of the $\text{LDOS}_x^{\text{ind}}(\mathbf{r}, \omega)$ calculated using Equation (6), as explained in the text. b) Value of $\langle G_{xx}^0 \rangle^2$ (dashed curves) and $\langle [G_{xx}^0]^2 \rangle$ (solid curves) as a function of d for the nanodisks of (a).

This expression assumes that the response of the nanodisk is completely concentrated at its center and therefore $|\mathbf{r} - \mathbf{r}'| = d$. However, we can improve its accuracy by replacing the square of the Green tensor with a better estimation. This can be done by computing its average value over the volume of the nanodisk and then taking the square $\langle G_{xx}^0 \rangle^2$, or, instead, by directly computing the average of the square $\langle [G_{xx}^0]^2 \rangle$. Both of these quantities encode the spatial extent of the electromagnetic fields and thus the efficiency with which the source and the nanodisks can couple. Inserting these quantities into Equation (6) and extracting $\text{Im}\{\alpha(\omega)\}$ from the dipolar limit of the extinction cross-section,^[66] $\sigma_{\text{ext}}(\omega) = 4\pi k \text{Im}\{\alpha(\omega)\}$, using the spectra of Figure 1a, we obtain the estimation of the peak value of $\text{LDOS}_x^{\text{ind}}(\mathbf{r}, \omega)$ shown by the shaded areas in Figure 3a. Specifically, the lower and upper bounds of these regions correspond to the results obtained using $\langle G_{xx}^0 \rangle^2$ and $\langle [G_{xx}^0]^2 \rangle$, respectively.

Expectedly, as d increases, the two estimations approach one another and the shaded area narrows due to the fact that the value of the Green tensor becomes more uniform over the volume of the nanodisk. Moreover, when d is small, the $\text{LDOS}_x^{\text{ind}}(\mathbf{r}, \omega)$ obtained from the FEM simulations (color dots) clearly lie within the bounds of the corresponding shaded area; however, for large d , the predictions of our approximate model slightly depart from the FEM results. The reason is that the electrostatic approximation that we use to compute the Green tensor becomes less accurate as kd grows. This effect is more

pronounced for the $t = 20$ nm, $D = 50$ nm nanodisk because its resonance is located at higher energies than those of the other two nanodisks under consideration.

Our simple model of the induced LDOS gives very important insight into the interplay between the intrinsic strength of the plasmon resonance of the nanodisk, measured by $\text{Im}\{\alpha(\omega)\}$, and the efficiency with which it is coupled to the near-field source, quantified by the averaged Green tensor. To analyze the coupling efficiency, we plot, in Figure 3b, the value of $\langle G_{xx}^0 \rangle^2$ (dashed curves) and $\langle [G_{xx}^0]^2 \rangle$ (solid curves) as a function of d for nanodisks with $t = 2$ nm, $D = 50$ nm (gray curves), $t = 5$ nm, $D = 125$ nm (red curves), and $t = 20$ nm, $D = 50$ nm (green curves). Examining these results, we observe that the thinnest nanodisk displays the largest values of both $\langle G_{xx}^0 \rangle^2$ and $\langle [G_{xx}^0]^2 \rangle$ for all distances under consideration, which can be attributed to a larger degree of confinement. As a consequence, the increased value of $\langle G_{xx}^0 \rangle^2$ and $\langle [G_{xx}^0]^2 \rangle$ is sufficient to compensate for the smaller value of $\text{Im}\{\alpha(\omega)\}$ displayed by the thinner nanodisks, as inferred from the extinction cross-section results shown in Figure 1a, and therefore produce a larger peak value of the induced LDOS. Therefore, from this analysis, we can conclude that the decrease of the near-field response of nanodisks with their thickness is a consequence of the change in the efficiency with which the near-field source couples with the dipolar plasmon mode of the nanodisk.

So far, we have considered nanodisks made of an ideal metal with a dielectric response described by a Drude model, which exclusively accounts for the effect of conduction electrons. This has allowed us to study how the plasmonic response of the nanodisks changes with their thickness t under near- and far-field excitation conditions. However, the dielectric response of real metals also contains a contribution from interband transitions associated with bound electrons, which mostly produces an increase in the absorption losses of the material. Therefore, it is important to understand the impact that interband transitions have on our analysis of the different thickness dependence of the near- and far-field response of metallic nanodisks. To this end, in Figure 4, we study the same three nanodisks of Figure 3 but using tabulated data for the dielectric function of gold compiled in ref. [67]. Specifically, Figure 4a,b show, respectively, the extinction cross-section and the induced LDOS.

Comparing the results for the nanodisks with $t = 2$ nm, $D = 50$ nm (gray curves) and $t = 5$ nm, $D = 125$ nm (red curves), we observe that they behave as expected: the peak value of $\sigma_{\text{ext}}(\omega)$ is larger for the thicker nanodisk, while the opposite is true for $\text{LDOS}_x^{\text{ind}}(\mathbf{r}, \omega)$. However, the peak value of the extinction cross-section of the nanodisk with $t = 20$ nm, $D = 50$ nm (green curves) is significantly smaller than that of the thinnest nanodisk. This can be explained from the fact that, while the lowest-order dipolar plasmons of the $t = 2$ nm, $D = 50$ nm and $t = 5$ nm, $D = 125$ nm nanodisks are located well below the interband transition threshold (≈ 2.3 eV) and therefore are not affected by them, the resonance of the $t = 20$ nm, $D = 50$ nm nanodisk clearly falls within it. As a consequence, the plasmon resonance suffers a larger level of losses that increases its width and consequently reduces its peak value. Therefore, we conclude that our analysis based on the Drude dielectric function remains valid for nanodisks made of real metals, as long as their plasmon resonances do not overlap with the interband transitions.

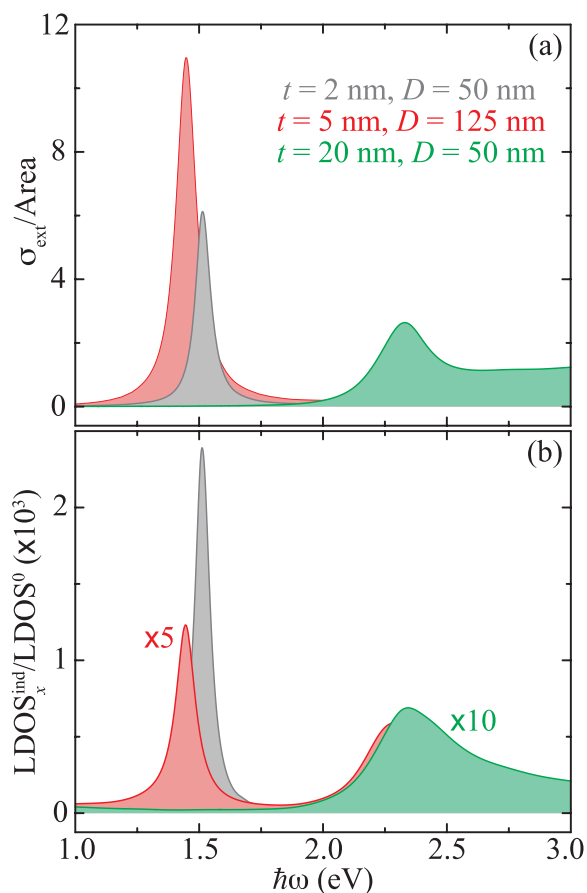


Figure 4. Analysis of the role of interband transitions. a) Normalized extinction cross-section of gold nanodisks with $t = 2 \text{ nm}$, $D = 50 \text{ nm}$ (gray curves), $t = 5 \text{ nm}$, $D = 125 \text{ nm}$ (red curves), and $t = 20 \text{ nm}$, $D = 50 \text{ nm}$ (green curves). b) $\text{LDOS}_x^{\text{ind}}(\mathbf{r}, \omega)$ normalized to LDOS^0 for the same nanodisks as in (a). Notice that in (b) the red and green curves have been multiplied by 5 and 10, respectively, to improve visibility.

3. Conclusions

In summary, using rigorous solutions of Maxwell's equations, we have analyzed the near- and far-field response of metallic nanodisks with varying thicknesses. We have found that, while the far-field response, quantified by the extinction cross-section, increases with the thickness, the opposite is true for the near-field response measured using the induced LDOS. This interesting behavior is observed both in cases where the thickness of the nanodisk is increased while its diameter is held constant and when, instead, its aspect ratio is kept fixed and thus there is a minimal shift in its resonance energy. Through an analysis of the induced charges on the surface of the nanodisks, we have shown that both near- and far-field sources excite the exact same dipolar plasmon, and, therefore, the different dependence with thickness can be attributed to the efficiency with which the mode is excited. To confirm this hypothesis, we have presented a simple model of the induced LDOS derived within the dipolar and electrostatic approximations. Using this model, which allows us to separate the intrinsic strength of the plasmon mode from the efficiency with which it couples to the source, we have shown that the coupling efficiency of thinner nanodisks is

sufficiently large to overcome the inherently stronger response of thicker nanodisks and therefore produce a larger near-field response. The results of our work provide fundamental insight into the optical properties of metallic nanostructures with high aspect ratios and thus can help to leverage these systems for applications that rely on both near- and far-field responses.

Supporting Information

Supporting Information is available from the Wiley Online Library or from the author.

Acknowledgements

L.Z. and P.G. contributed equally to this work. This work was sponsored by Grant No. TEM-FLU PID2019-109502GA-I00 funded by MCIN/AEI/10.13039/501100011033 and the U.S. National Science Foundation (Grant No. DMR-1941680). L.Z. acknowledges support from the Department of Energy Computational Science Graduate Fellowship (Grant No. DE-SC0020347). P.G. thanks financial support from the UNM NSMS program through the Whitten Family Fellowship and the Graduate Assistance in Areas of National Need (GAANN) fellowship.

Conflict of Interest

The authors declare no conflict of interest.

Data Availability Statement

The data that support the findings of this study are available from the corresponding author upon reasonable request.

Keywords

2D materials, far-field excitation, nanodisks, near-field excitation, plasmonic response, sum rule, thin metallic nanostructures

Received: November 23, 2021

Revised: February 7, 2022

Published online:

- [1] S. A. Maier, *Plasmonics: Fundamentals and Applications*, Springer, New York **2007**.
- [2] J. A. Schuller, E. S. Barnard, W. Cai, Y. C. Jun, J. S. White, M. L. Brongersma, *Nat. Mater.* **2010**, *9*, 193.
- [3] R. A. Álvarez-Puebla, L. M. Liz-Marzán, F. J. García de Abajo, *J. Phys. Chem. Lett.* **2010**, *1*, 2428.
- [4] H. Xu, E. J. Bjerneld, M. Käll, L. Börjesson, *Phys. Rev. Lett.* **1999**, *83*, 4357.
- [5] J. N. Anker, W. P. Hall, O. Lyandres, N. C. Shah, J. Zhao, R. P. Van Duyne, *Nat. Mater.* **2008**, *7*, 442.
- [6] S.-Y. Ding, E.-M. You, Z.-Q. Tian, M. Moskovits, *Chem. Soc. Rev.* **2017**, *46*, 4042.
- [7] K. R. Catchpole, A. Polman, *Opt. Express* **2008**, *16*, 21793.
- [8] H. A. Atwater, A. Polman, *Nat. Mater.* **2010**, *9*, 205.
- [9] G. Baffou, R. Quidant, *Chem. Soc. Rev.* **2014**, 3898.

- [10] M. L. Brongersma, N. J. Halas, P. Nordlander, *Nat. Nanotechnol.* **2015**, *10*, 25.
- [11] Y.-J. Lu, J. Kim, H.-Y. Chen, C. Wu, N. Dabidian, C. E. Sanders, C.-Y. Wang, M.-Y. Lu, B.-H. Li, X. Qiu, W.-H. Chang, L.-J. Chen, G. Shvets, C.-K. Shih, S. Gwo, *Science* **2012**, *337*, 450.
- [12] A. Yang, T. W. Odom, *IEEE Photonics J.* **2015**, *7*, 0700606.
- [13] A. H. Castro Neto, F. Guinea, N. M. R. Peres, K. S. Novoselov, A. K. Geim, *Rev. Mod. Phys.* **2009**, *81*, 109.
- [14] F. H. L. Koppens, D. E. Chang, F. J. García de Abajo, *Nano Lett.* **2011**, *11*, 3370.
- [15] Z. Fei, G. O. Andreev, W. Bao, L. M. Zhang, A. S. McLeod, C. Wang, M. K. Stewart, Z. Zhao, G. Dominguez, M. Thiemens, M. M. Fogler, M. J. Tauber, A. H. Castro-Neto, C. N. Lau, F. Keilmann, D. N. Basov, *Nano Lett.* **2011**, *11*, 4701.
- [16] J. Chen, M. Badioli, P. Alonso-González, S. Thongrattanasiri, F. Huth, J. Osmond, M. Spasenović, A. Centeno, A. Pesquera, P. Godignon, A. Zurutuza Elorza, N. Camara, F. J. García de Abajo, R. Hillenbrand, F. H. L. Koppens, *Nature* **2012**, *487*, 77.
- [17] Z. Fei, A. S. Rodin, G. O. Andreev, W. Bao, A. S. McLeod, M. Wagner, L. M. Zhang, Z. Zhao, M. Thiemens, G. Dominguez, M. M. Fogler, A. H. C. Neto, C. N. Lau, F. Keilmann, D. N. Basov, *Nature* **2012**, *487*, 82.
- [18] A. N. Grigorenko, M. Polini, K. S. Novoselov, *Nat. Photonics* **2012**, *6*, 749.
- [19] F. J. García de Abajo, *ACS Photonics* **2014**, *1*, 135.
- [20] T. Nagao, G. Han, C. Hoang, J.-S. Wi, A. Pucci, D. Weber, F. Neubrech, V. M. Silkin, D. Enders, O. Saito, M. Rana, *Sci. Technol. Adv. Mater.* **2010**, *11*, 054506.
- [21] A. Manjavacas, F. J. García de Abajo, *Nat. Commun.* **2014**, *5*, 3548.
- [22] C. V. Hoang, M. Rana, T. Nagao, *Appl. Phys. Lett.* **2014**, *104*, 251117.
- [23] X. Li, A. Teng, M. M. Özer, J. Shen, H. H. Weitering, Z. Zhang, *New J. Phys.* **2014**, *16*, 065014.
- [24] F. J. García de Abajo, A. Manjavacas, *Faraday Discuss.* **2015**, *178*, 87.
- [25] A. Kossov, V. Merk, D. Simakov, K. Leosson, S. Kéna-Cohen, S. A. Maier, *Adv. Opt. Mater.* **2015**, *3*, 71.
- [26] D. Shah, H. Reddy, N. Kinsey, V. M. Shalaev, A. Boltasseva, *Adv. Opt. Mater.* **2017**, *5*, 1700065.
- [27] I. V. Bondarev, V. M. Shalaev, *Opt. Mater. Express* **2017**, *7*, 3731.
- [28] M. Z. Herrera, A. K. Kazansky, J. Aizpurua, A. G. Borisov, *Phys. Rev. B* **2017**, *95*, 245413.
- [29] D. Shah, A. Catellani, H. Reddy, N. Kinsey, V. Shalaev, A. Boltasseva, A. Calzolari, *ACS Photonics* **2018**, *5*, 2816.
- [30] L. J. Kraye, J. Kim, J. N. Munday, *Opt. Mater. Express* **2019**, *9*, 330.
- [31] A. Boltasseva, V. M. Shalaev, *ACS Photonics* **2019**, *6*, 1.
- [32] Z. M. Abd El-Fattah, V. Mkhitarian, J. Brede, L. Fernández, C. Li, Q. Guo, A. Ghosh, A. R. Echarri, D. Naveh, F. Xia, J. E. Ortega, F. J. García de Abajo, *ACS Nano* **2019**, *13*, 7771.
- [33] R. Sundararaman, T. Christensen, Y. Ping, N. Rivera, J. D. Joannopoulos, M. Soljačić, P. Narang, *Phys. Rev. Mater.* **2020**, *4*, 074011.
- [34] D. Shah, Z. A. Kudyshev, S. Saha, V. M. Shalaev, A. Boltasseva, *MRS Bull.* **2020**, *45*, 188.
- [35] F. Moresco, M. Rocca, T. Hildebrandt, M. Henzler, *Phys. Rev. Lett.* **1999**, *83*, 2238.
- [36] A. Rodríguez Echarri, J. D. Cox, F. J. García de Abajo, *Optica* **2019**, *6*, 630.
- [37] F. Aguilón, D. C. Marinica, A. G. Borisov, *J. Phys. Chem. C* **2020**, *124*, 28210.
- [38] I. V. Bondarev, H. Mousavi, V. M. Shalaev, *Phys. Rev. Res.* **2020**, *2*, 013070.
- [39] Y. Muniz, A. Manjavacas, C. Farina, D. A. R. Dalvit, W. J. M. Kort-Kamp, *Phys. Rev. Lett.* **2020**, *125*, 033601.
- [40] N. Rivera, I. Kaminer, B. Zhen, J. D. Joannopoulos, M. Soljačić, *Science* **2016**, *353*, 263.
- [41] S. Sanders, A. May, A. Alessandro, A. Manjavacas, *ACS Photonics* **2018**, *5*, 4022.
- [42] A. Ciattoni, C. Conti, A. Marini, *Commun. Phys.* **2019**, *2*, 111.
- [43] E. J. C. Dias, R. Yu, F. J. García de Abajo, *Light Sci. Appl.* **2020**, *9*, 87.
- [44] R. A. Maniyara, D. Rodrigo, R. Yu, J. Canet-Ferrer, D. S. Ghosh, R. Yongsunthon, D. E. Baker, A. Rezikyan, F. J. García de Abajo, V. Pruneri, *Nat. Photonics* **2019**, *13*, 328.
- [45] H.-T. Chen, A. J. Taylor, N. Yu, *Rep. Prog. Phys.* **2016**, *79*, 076401.
- [46] Y. H. Jang, Y. J. Jang, S. Kim, L. N. Quan, K. Chung, D. H. Kim, *Chem. Rev.* **2016**, *116*, 14982.
- [47] A. J. Moilanen, T. K. Hakala, P. Törmä, *ACS Photonics* **2018**, *5*, 54.
- [48] D. G. Baranov, M. Wersäll, J. Cuadra, T. J. Antosiewicz, T. Shegai, *ACS Photonics* **2018**, *5*, 24.
- [49] J. T. Hugall, A. Singh, N. F. van Hulst, *ACS Photonics* **2018**, *5*, 43.
- [50] A. Manjavacas, S. Thongrattanasiri, D. E. Chang, F. J. García de Abajo, *New J. Phys.* **2012**, *14*, 123020.
- [51] M. W. Chu, V. Myroshnychenko, C. H. Chen, J. P. Deng, C. Y. Mou, F. J. García de Abajo, *Nano Lett.* **2009**, *9*, 399.
- [52] D. E. Gómez, Z. Q. Teo, M. Altissimo, T. J. Davis, S. Earl, A. Roberts, *Nano Lett.* **2013**, *13*, 3722.
- [53] R. Yu, L. M. Liz-Marzán, F. J. García de Abajo, *Chem. Soc. Rev.* **2017**, *46*, 6710.
- [54] L. Novotny, B. Hecht, *Principles of Nano-Optics*, Cambridge University Press, New York **2006**.
- [55] K. Joulain, R. Carminati, J. P. Mulet, J. J. Greffet, *Phys. Rev. B* **2003**, *68*, 245405.
- [56] D. P. Fussell, R. C. McPhedran, C. Martijn de Sterke, *Phys. Rev. E* **2004**, *70*, 066608.
- [57] R. Carminati, A. Cazé, D. Cao, F. Peragut, V. Krachmalnicoff, R. Pierrat, Y. D. Wilde, *Surf. Sci. Rep.* **2015**, *70*, 1.
- [58] T. V. Shahbazyan, *Phys. Rev. Lett.* **2016**, *117*, 207401.
- [59] S. Sanders, A. Manjavacas, *ACS Photonics* **2018**, *5*, 2437.
- [60] A. Dereux, C. Girard, J.-C. Weeber, *J. Chem. Phys.* **2000**, *112*, 7775.
- [61] R. Carminati, J.-J. Greffet, C. Henkel, J. Vigoureux, *Opt. Commun.* **2006**, *261*, 368.
- [62] W. Kuhn, *Z. Phys.* **1925**, *33*, 408.
- [63] F. Reiche, W. Thomas, *Z. Phys.* **1925**, *34*, 510.
- [64] Z.-J. Yang, T. J. Antosiewicz, R. Verre, F. J. García de Abajo, S. P. Apell, M. Käll, *Nano Lett.* **2015**, *15*, 7633.
- [65] A. Delga, J. Feist, J. Bravo-Abad, F. J. Garcia-Vidal, *Phys. Rev. Lett.* **2014**, *112*, 253601.
- [66] V. Myroshnychenko, J. Rodríguez-Fernández, I. Pastoriza-Santos, A. M. Funston, C. Novo, P. Mulvaney, L. M. Liz-Marzán, F. J. García de Abajo, *Chem. Soc. Rev.* **2008**, *37*, 1792.
- [67] P. B. Johnson, R. W. Christy, *Phys. Rev. B* **1972**, *6*, 4370.

ADVANCED OPTICAL MATERIALS

Supporting Information

for *Adv. Optical Mater.*, DOI: 10.1002/adom.202102550

Comparative Analysis of the Near- and Far-Field Optical
Response of Thin Plasmonic Nanostructures

*Lauren Zundel, Paul Gieri, Stephen Sanders, and
Alejandro Manjavacas**

Supporting Information

Comparative Analysis of the Near- and Far-Field Optical Response of Thin Plasmonic Nanostructures

Lauren Zundel^{1,||}, *Paul Gieri*^{1,||}, *Stephen Sanders*¹, and *Alejandro Manjavacas*^{2,1*}

¹Department of Physics and Astronomy, University of New Mexico, Albuquerque, New Mexico 87106, United States

²Instituto de Óptica (IO-CSIC), Consejo Superior de Investigaciones Científicas, 28006 Madrid, Spain

Email: a.manjavacas@csic.es

^{||}These authors contributed equally

Finite Element Method Calculations

The calculations of the extinction, induced LDOS, and induced charges presented in the main paper are obtained by rigorously solving Maxwell's equations using the finite element method (FEM) implemented in the commercial software COMSOL Multiphysics. In particular, we construct each of the nanodisks from the revolution about the z -axis of a rectangle of size $(D/2) \times t$ with corners rounded with a radius of curvature of 0.4 nm. The nanodisk is placed at the center of a rectangular prism that constitutes the simulation domain. In order to reduce the computational cost of the calculations, we cut the simulation domain through the center of the nanodisk in the xz - and yz -planes, using perfect magnetic and perfect electric conductor boundaries, respectively. All other boundaries of the domain are truncated with perfectly matched layers (PMLs).

To calculate the extinction cross-section, we set a linearly polarized plane wave as the background field. Once we have calculated the field at all points in the simulation domain, the extinction cross-section is found from the sum of the scattering cross-section, obtained from the integral of the Poynting vector over the surface of the nanodisk, and the absorption cross-section, obtained by integrating the power dissipated in the nanodisk volume. On the other hand, to calculate the LDOS, we place an x -polarized electric point dipole on the z -axis a distance d above the surface of the nanodisk and compute the imaginary part of the electric field at the position of the dipole. By doing so, we obtain, up to a constant factor, $\text{Im}\{\mathbf{G}(\mathbf{r}, \mathbf{r}, \omega)\}$, from which the induced LDOS can be computed using Equation (3) of the main paper. Finally, to calculate the induced charges, we compute the difference between the normal component of the electric field directly above and below the surface of the nanodisk. All of the calculations have been checked for convergence with respect to mesh and domain size.

Analysis of the Dipolar Modes of the Nanodisks

In the main paper, we focused on the first-order dipolar mode of the different nanodisks. However, the nanostructures support higher-order dipolar modes, which we analyze in **Figure S1**. In particular, the gray curve in Figure S1a shows the normalized LDOS _{x} ^{ind}(\mathbf{r}, ω) of the nanodisk with $t = 2$ nm and diameter $D = 50$ nm of Figure 1b of the main paper, calculated over an expanded range of energies. The upper insets show the induced charges at the peak frequencies of the three modes with the highest energy and the three with the lowest, as indicated by the dashed arrows. We can clearly distinguish two types of modes based on the symmetry of the charge distribution with respect to the xy -plane: symmetric modes, in which the signs of the induced charge on the top and the bottom surfaces of the nanodisk are the same, and antisymmetric

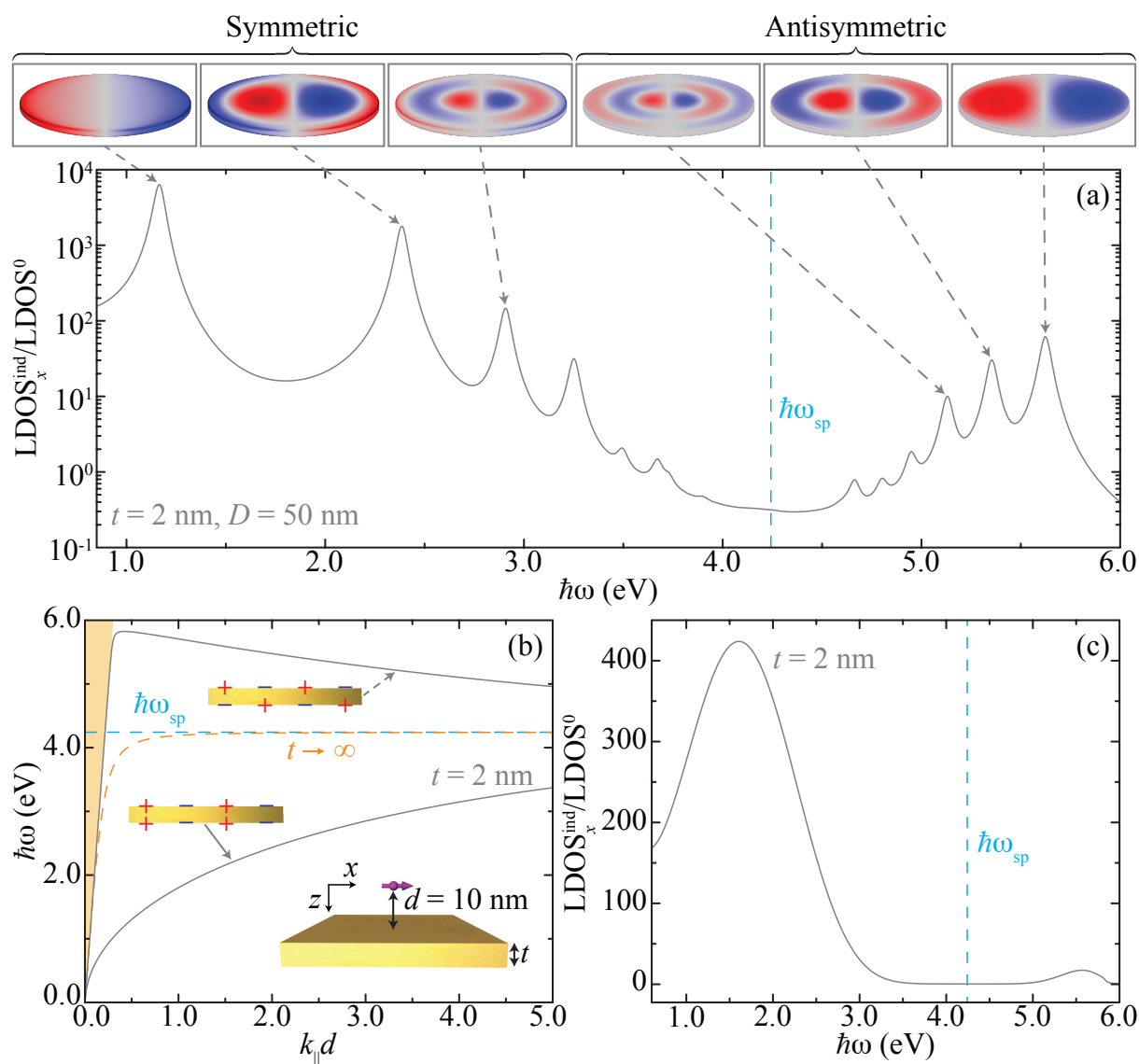


Figure S1. Analysis of modes of a nanodisk and extended thin film. a) Higher-order dipolar modes of a nanodisk. The gray curve shows the normalized LDOS_x^{ind}(\mathbf{r}, ω) calculated at a distance $d = 10$ nm above the center of the surface of a nanodisk with thickness $t = 2$ nm and diameter $D = 50$ nm. The upper insets display the spatial profile of induced charges in the nanodisk at the frequencies of the various modes, as indicated by the dashed arrows. b) Dispersion relation for an extended thin film with thickness $t = 2$ nm (solid gray curves) and $t \rightarrow \infty$ (dashed orange curve), as depicted in the inset schematics. The shaded yellow area marks the light cone. c) Normalized LDOS_x^{ind}(\mathbf{r}, ω) calculated at a distance $d = 10$ nm for an extended film with thickness $t = 2$ nm. In all panels, the characteristic surface plasmon energy $\hbar\omega_{sp} = \hbar\omega_p/\sqrt{2}$ is marked by the blue dashed line.

modes, in which the signs are opposite. The symmetric modes all occur at energies below $\hbar\omega_{\text{sp}} = \hbar\omega_{\text{p}}/\sqrt{2}$, the characteristic surface plasmon energy of the material [1] (marked by the blue dashed line), while the asymmetric ones are located at higher energies. In addition, the number of nodes in the radial direction increases for both the symmetric and antisymmetric modes as they get closer to $\hbar\omega_{\text{sp}}$.

The split of symmetric and antisymmetric nodes around $\hbar\omega_{\text{sp}}$ resembles the behavior of the modes of an extended thin film [1]. As shown in Figure S1b, this system supports two modes (gray curves), one symmetric and the other antisymmetric, whose energies, for a given value of the component of the wavevector parallel to the film k_{\parallel} are, respectively, above and below the energy of the surface plasmon polariton of a semi-infinite medium (orange dashed curve). This resemblance is completely expected from the fact that an extended thin film can be considered as the limit of a nanodisk with $D/t \rightarrow \infty$. To complete our comparison, we show the normalized induced LDOS [2] of the $t = 2$ nm film in Figure S1c. As expected, the spectrum shows two modes, one on either side of $\hbar\omega_{\text{sp}}$.

References

- [1] S. A. Maier, *Plasmonics: Fundamentals and Applications*, Springer, New York, **2007**.
- [2] L. Novotny, B. Hecht, *Principles of Nano-Optics*, Cambridge University Press, New York, **2006**.